

# The Endgame of Gas Giant Formation: Accretion Luminosity and Contraction Post-Runaway

Sivan Ginzburg<sup>1</sup><sup>★</sup><sup>†</sup> and Eugene Chiang<sup>1,2</sup>

<sup>1</sup>*Department of Astronomy, University of California at Berkeley, CA 94720-3411, USA*

<sup>2</sup>*Department of Earth and Planetary Science, University of California at Berkeley, CA 94720-4767, USA*

Accepted XXX. Received YYY; in original form ZZZ

## ABSTRACT

Giant planets are thought to form by runaway gas accretion onto solid cores. Growth must eventually stop running away, ostensibly because planets open gaps (annular cavities) in their surrounding discs. Typical models stop runaway by artificially capping the accretion rate and lowering it to zero over an arbitrarily short time-scale. In reality, post-runaway accretion persists as long as the disc remains. During this final and possibly longest phase of formation, when the planet is still emerging from the disc, its mass can more than double, and its radius contracts by orders of magnitude. By drawing from the theory of how gaps clear, we find that post-runaway accretion luminosities diverge depending on disc viscosity: luminosities fall in low-viscosity discs but continue to rise past runaway in high-viscosity discs. This divergence amounts to a factor of  $10^2$  by the time the disc disperses. Irrespective of the specifics of how planets interact with discs, the observed luminosity and age of an accreting planet can be used to calculate its instantaneous mass, radius, and accretion rate. We perform this exercise for the planet candidates embedded within the discs orbiting PDS 70, HD 163296, and MWC 758, inferring masses of 1–10  $M_J$ , accretion rates of 0.1–10  $M_J/\text{Myr}$ , and radii of 1–10  $R_J$ . Our radii are computed self-consistently from the planet’s concurrent contraction and accretion and do not necessarily equal the value of  $2R_J$  commonly assumed; in particular, the radius depends on the envelope opacity as  $R \propto \kappa^{0.5}$ .

**Key words:** planets and satellites: formation – planets and satellites: gaseous planets

## 1 INTRODUCTION

The leading theory for the formation of giant planets is the core accretion model, in which a rocky or icy core several times the mass of Earth gravitationally accretes a gas atmosphere from an ambient circumstellar disc (Perri & Cameron 1974; Harris 1978; Mizuno et al. 1978; Mizuno 1980; Stevenson 1982; Bodenheimer & Pollack 1986; Pollack et al. 1996). Initially, the bottleneck for gas accretion is the atmosphere’s Kelvin–Helmholtz (KH) cooling time, i.e. how long atmospheric gas takes to radiate away its gravitational energy, thereby contracting onto the core and allowing fresh nebular gas to take its place (e.g. Piso & Youdin 2014). This cooling time, which sets the atmosphere’s mass-doubling rate, increases as the atmosphere grows (e.g. Lee & Chiang 2015). Once the atmosphere and core become comparable in mass and atmospheric self-gravity can no longer be neglected, the KH growth time decreases with increasing mass: the planet accumulates

mass over ever shorter time-scales in a ‘runaway’ growth phase (Bodenheimer & Pollack 1986; Pollack et al. 1996; Ikoma et al. 2000; Lee et al. 2014; Piso & Youdin 2014; Lee & Chiang 2015; Piso et al. 2015; Ginzburg & Chiang 2019, and references therein). During pre-runaway and runaway, the radius of a nascent gas giant is several orders of magnitude larger than the radius of Jupiter  $R_J$ , as the planet’s atmosphere extends to the Bondi radius (or the Hill radius if it is smaller) where it connects to the external nebula (Bodenheimer et al. 2000).

At some stage, the nebula is unable to supply gas at a sufficient rate to keep pace with the continuously shortening cooling time-scale. Accretion then becomes controlled hydrodynamically rather than thermodynamically. Ginzburg & Chiang (2019, hereafter GC19) considered the hydrodynamics of gas flows in the sub-thermal regime, appropriate for planets whose Bondi radii are less than their Hill radii (which in turn are less than the disc pressure scale height). For sub-thermal planets—these could be to up to several times the mass of Jupiter  $M_J$  in the outermost portions of discs, beyond 10 au—the hydrodynamic accretion rate should be given by Bondi (e.g. Edgar 2004). At fixed

<sup>★</sup> E-mail: ginzburg@berkeley.edu

<sup>†</sup> 51 Pegasi b Fellow.

ambient disc density, growth at the Bondi rate still runs away, as the mass-doubling time-scale continues to decrease with increasing mass.

What stops runaway may be the opening of gaps: annular depletions of disc density around the planet’s orbit effected by repulsive Lindblad torques (Goldreich & Tremaine 1980; Goodman & Rafikov 2001; Ginzburg & Sari 2018). The more massive the planet, the deeper the gap it excavates and the more it staves off its mass supply (Lin & Papaloizou 1993; Bryden et al. 1999; Kley 1999; Lubow et al. 1999; D’Angelo et al. 2003; Tanigawa & Ikoma 2007; Lissauer et al. 2009; Machida et al. 2010; Tanigawa & Tanaka 2016; Lee 2019); this negative feedback loop lengthens the mass-doubling time-scale until it exceeds the gas disc lifetime of a few million years (Mamajek 2009; Williams & Cieza 2011; Alexander et al. 2014). Throttling of gas accretion is most severe in low-viscosity discs where gaps are deepest (GC19, and references therein).

Our goal here is to calculate how the radius  $R$  and luminosity  $L$  of a planet evolve during this last phase of nebular accretion, after the planet transitions out of runaway. How does a planet shrink from its Bondi radius, and what is its peak luminosity, still powered by residual accretion? Our calculation applies directly to planets just emerging from and still feeding off their parent discs, of which there are now several candidates directly imaged (Sallum et al. 2015; Guidi et al. 2018; Reggiani et al. 2018; Wagner et al. 2018; Haffert et al. 2019). We will estimate the masses and accretion rates of these objects.

While our analysis is directly inspired by a modern understanding of how gaps open in discs, we keep much of our treatment general by using a simple power-law parametrization of post-runaway accretion that can be adjusted to model different disc-planet interaction scenarios. Regardless of the details of any particular scenario, post-runaway accretion should play out naturally over the lifetime of the gas disc—and so we will find planet contraction and luminosity histories unfolding over the same long time-scale of Myrs (by contrast to earlier, artificially short accretion prescriptions made for computational convenience; see section 2.1 of Marley et al. 2007). Most of the planet’s contraction, amounting to orders-of-magnitude reduction in radius, occurs during this final stage of nebular accretion.

The rest of this paper is organized as follows. In Section 2 we review how cooling-limited accretion runs away. The subsequent hydrodynamically-limited phase, when accretion continues through gaps, is discussed in Section 3. There we describe our method for calculating the post-runaway radius, luminosity, and effective temperature. Section 4 presents the resultant evolutionary tracks, both as functions of mass and of time, with dependences on opacity noted in Section 5. Applications to observations are made in Section 6, after which we summarize and provide an outlook in Section 7.

## 2 RUNAWAY COOLING

The cooling-limited phase of gas accretion onto planetary cores has been studied extensively, with an emphasis on pre-runaway accretion, when the planet’s gas atmosphere is lighter than the core (Pollack et al. 1996; Ikoma et al. 2000;

Papaloizou & Nelson 2005; Rafikov 2006; Lee et al. 2014; Piso & Youdin 2014; Lee & Chiang 2015; Piso et al. 2015; Ginzburg et al. 2016; Lee et al. 2018). In GC19 we extended the analytical scaling relations of pre-runaway cooling to the runaway regime, when the atmosphere surpasses the core in mass and dominates the gravitational field. Here we repeat and expand upon the calculation of runaway cooling. We omit order-unity coefficients to concentrate on scaling relations.

During runaway, most of the nascent giant’s mass  $M$  resides in its self-gravitating convective atmosphere (an ideal-gas polytrope with an adiabatic index  $\gamma$ ). The convective interior is overlaid by a radiative layer whose temperature varies by a factor of order unity from the surrounding nebula’s temperature  $T_0$ . We define the planet’s radius  $R$  as the location of the radiative–convective boundary (rcb). The planet’s accretion rate is initially given by the KH cooling time-scale  $t_{\text{cool}} \equiv E/L$ . The gravitational energy to be radiated away is  $E \sim GM^2/R$  where  $G$  is the gravitational constant, and the luminosity follows from applying the diffusion equation to the radiative layer:  $L \sim 4\pi R^2 \sigma T_0^4 / \tau$ , where  $\sigma$  is the Stefan–Boltzmann constant and  $\tau$  is the optical depth at the rcb measured radially from the outside in (for power-law opacities,  $T^4$  changes by an order-unity factor across the radiative layer; e.g. Rafikov 2006; Piso & Youdin 2014; Ginzburg & Sari 2015).

From hydrostatic equilibrium, the temperature at the planet’s centre is given by  $k_B T_c \sim GM\mu/R$ , where  $k_B$  is Boltzmann’s constant and  $\mu$  is the mean molecular weight. The central density of the polytrope is given by  $\rho_c \sim M/R^3$ . We use the adiabatic relation  $\rho \propto T^{1/(\gamma-1)}$  to calculate the density at the rcb:

$$\rho_{\text{rcb}} = \frac{M}{R^3} \left( \frac{k_B T_0 R}{GM\mu} \right)^{1/(\gamma-1)} = \frac{M}{R^3} \left( \frac{R}{R_B} \right)^{1/(\gamma-1)}, \quad (1)$$

where

$$R_B = \frac{GM\mu}{k_B T_0} \quad (2)$$

is the Bondi radius, and where we substituted  $T_0$  for the temperature at the rcb. The optical depth at the rcb is

$$\tau = \kappa \rho_{\text{rcb}} h = \frac{\kappa M}{RR_B} \left( \frac{R}{R_B} \right)^{1/(\gamma-1)}, \quad (3)$$

where  $\kappa$  and  $h = R^2/R_B$  are the local opacity and scale height, respectively. The cooling time-scale is therefore

$$t_{\text{cool}} = \frac{E}{L} = \left( \frac{k_B}{\mu} \right)^5 \frac{\kappa}{4\pi\sigma G^4} \frac{T_0}{M^2} \left( \frac{R_B}{R} \right)^{(4\gamma-5)/(\gamma-1)}. \quad (4)$$

We adopt a nominal disc temperature of  $T_0 = 100$  K for consistency with GC19. As explained below, our main results are independent of this choice. We assume for simplicity a nominal constant rcb dust opacity  $\kappa = 0.1 \text{ cm}^2 \text{ g}^{-1}$ , neglecting weak dependences on temperature and density in the relevant parameter range (Bell & Lin 1994; Piso et al. 2015);<sup>1</sup> we also test a lower dust-free opacity in Section 5. We take  $\mu = 2$  amu, appropriate for molecular hydrogen at the rcb.

<sup>1</sup> Specifically, we are motivated by the nominal opacities of Piso et al. (2015), as given by the dashed red line in their fig. 16; these account for grain growth following D’Alessio et al. (2001).

As long as KH cooling is the bottleneck for gas accretion,  $R \sim R_B$  to within a logarithmic factor (Piso & Youdin 2014; Ginzburg et al. 2016); in other words, the rcb scales with the atmosphere’s outer boundary, which is located at  $R_B$  for the wide-orbit planets of interest here (see GC19). Hence, during this stage the planet’s radius increases as  $R \propto M$  and its luminosity as  $L \propto M^3$ . The growth time decreases as  $t_{\text{cool}} \propto M^{-2}$  according to equation (4), indicating runaway gas accretion.

We note that as long as  $R \sim R_B$ , the planet’s interior temperature is of order  $T_0$ , implying that  $\gamma = 7/5$  (hydrogen is molecular) throughout the planet. As the planet contracts and heats up in later stages,  $\gamma$  varies spatially, necessitating a numerical integration (Section 3.1).

### 3 HYDRODYNAMIC REGULATION

While KH cooling is one limit to the planet’s growth rate, another is the nebula’s ability to supply the planet with fresh gas. We parametrize the hydrodynamical mass-doubling time-scale with a power law  $t_{\text{hydro}} \equiv M/\dot{M} \propto M^\beta$ ; this is equivalent to a parametrization of the accretion rate  $\dot{M}$  with time. In GC19 we found that Bondi accretion through a planet-carved gap corresponds to  $\beta = 3$  in viscous discs (Shakura & Sunyaev 1973 viscosity parameters  $\alpha \gtrsim 10^{-3}$ ) and  $\beta \approx 15$  in nearly inviscid ones ( $\alpha \lesssim 10^{-3}$ ). These results were obtained by calculating the time history of gap depletion by the planet’s repulsive gravitational torque. In Section 4 we examine  $\beta = 3$  and  $\beta = 15$  as fiducial cases, and demonstrate that the two values lead to qualitatively different outcomes. In Section 6 we treat  $\dot{M}$  as a free function to explore other limiting mechanisms, also hydrodynamical but not necessarily involving gaps (Szulágyi et al. 2014; Tanigawa & Tanaka 2016).

Because  $t_{\text{cool}} \propto M^{-2}$  (during runaway) and  $t_{\text{hydro}} \propto M^\beta$  where  $\beta$  is generally positive, there is a transition point when the time-scales cross and accretion becomes limited hydrodynamically rather than thermodynamically (see fig. 1 of GC19). We denote by  $M_0$  the planet mass at this transition:

$$t_{\text{hydro}} \equiv \frac{M}{\dot{M}} = t_{\text{cool}}(M_0) \left( \frac{M}{M_0} \right)^\beta. \quad (5)$$

The transition marks the end of runaway and the starting point for the calculations in the remainder of this paper. For simplicity, unless otherwise indicated, we adopt a fixed  $M_0 = 0.5M_J$ , characteristic of values computed in GC19.<sup>2</sup> The parametrization in equation (5) enables us to study the sensitivity of our results to both  $\beta$  and the minimum growth time  $t_{\text{cool}}(M_0)$  (evaluated using equation 4 with  $R = R_B$ ).

We now show that after the transition, post-runaway, the planet adjusts so that  $t_{\text{cool}} = t_{\text{hydro}}$ . Suppose this were not true, that just after the transition  $t_{\text{cool}} < t_{\text{hydro}}$ . For times  $t_{\text{cool}} < t < t_{\text{hydro}}$ , the planet radiates away its gravitational energy and undergoes KH contraction while initially keeping a constant mass (since growth is throttled

on the longer time-scale  $t_{\text{hydro}}$ ). The planet thus detaches from the nebula as  $R < R_B$  (see also Bodenheimer et al. 2000; Marley et al. 2007). Now according to equation (4), as the planet contracts,  $t_{\text{cool}} \propto R^{-(4\gamma-5)/(\gamma-1)} \propto R^{-3/2}$  increases. Eventually  $t_{\text{cool}}$  reaches  $t_{\text{hydro}}$  (whose value does not depend on  $R$ ), whereupon the planet resumes its growth. We conclude that post-runaway, the planet grows and contracts simultaneously (see Fig. 1) while satisfying the condition  $t_{\text{cool}} = t_{\text{hydro}}$ .

#### 3.1 Numerical scheme for $R(M)$

The planet’s contraction during its post-runaway growth  $R(M)$  can be calculated by solving  $t_{\text{cool}}(M, R) = t_{\text{hydro}}(M)$ . This equation has to be solved numerically, since  $\gamma$  is not uniform as hydrogen dissociates and ionizes during the planet’s contraction and heating. We now describe our general solution scheme, and defer to the appendix analytical solutions for some asymptotic cases.

The planet’s post-runaway evolution is divided into two successive stages. During the first stage, the planet remains partitioned by an rcb (Section 3.1.1), while in the second stage it is fully convective (Section 3.1.2). These stages correspond to the ‘stalling’ and ‘cooling’ regimes in section 4.2 of Berardo et al. (2017).

##### 3.1.1 Post-runaway stage 1: radiative envelope

We denote by  $T$  the temperature at the planet’s photosphere. Initially,  $T$  equals the nebular temperature  $T_0$ , and the planet is engulfed by a thick, radiative, and nearly isothermal envelope of optical depth  $\tau \gg 1$ , similar to conditions during runaway (Section 2). Now as then, the central temperature and density are given by  $k_B T_c = GM\mu/R$  and  $\rho_c = M/R^3$ . We take the temperature at the rcb to be identical to the photospheric temperature  $T$ , and find the rcb density  $\rho_{\text{rcb}}$  by numerically integrating

$$\frac{d \ln \rho}{d \ln T'} = \frac{1}{\gamma(\rho, T') - 1} \quad (6)$$

from  $(T_c, \rho_c)$  to  $(T, \rho_{\text{rcb}})$  using a fourth-order Runge–Kutta method. The adiabatic index  $\gamma$  is given by equations (B2) and (B3) of Piso et al. (2015), supplemented by the Saha equation for calculating the fractions of molecular, atomic, and ionized hydrogen. In Section 4 we detail how hydrogen transitions from molecular ( $\gamma = 7/5$ ) to atomic ( $\gamma = 5/3$ ) within the planet’s evolving envelope, with  $\gamma$  dropping in regions of partial dissociation or ionization as energy goes into breaking molecules or atoms instead of heat (Saumon et al. 1995; Lee et al. 2014; Piso et al. 2015). Having solved for  $\rho_{\text{rcb}}$ , we estimate the optical depth at the rcb as

$$\tau(M, R, T) = \rho_{\text{rcb}} \kappa h \quad (7)$$

where  $h = (k_B T R^2)/(GM\mu)$  is the scale height there.

The planet cools with luminosity

$$L = \frac{4\pi R^2 \sigma T_0^4}{\tau} = \frac{GM^2}{t_{\text{hydro}} R}, \quad (8)$$

where the second equality follows from  $t_{\text{cool}} = t_{\text{hydro}}$  (see the paragraph just before Section 3.1). It follows that the optical

<sup>2</sup> Equating equations (9) and (18) of GC19, and assuming their disc model, we find  $M_0 \propto M_{\text{disc}}^{0.2} \kappa^{0.2} \alpha^{0.28} a^{0.09}$  for  $\beta = 3$  and  $M_0 \propto M_{\text{disc}}^{0.29} \kappa^{0.06} \alpha^{0.64}$  for  $\beta = 15$ ;  $a$  is the planet’s orbital radius and  $M_{\text{disc}}$  is the total mass of the disc, which determines its density normalization.

depth must also satisfy

$$\tau(M, R, T_0) = \frac{4\pi R^3 \sigma T_0^4 t_{\text{hydro}}(M)}{GM^2}. \quad (9)$$

We solve equation (9) numerically for  $R(M)$ , calculating the left-hand side using equation (7) independently of the right-hand side.

We note in passing that for the radius to shrink from  $R_B$  to much smaller values (smaller by two orders of magnitude according to Fig. 1), the planet almost certainly has to find a way to shed its spin angular momentum. Possible mechanisms for angular momentum loss include expulsion of material into a circumplanetary disc (Ward & Canup 2010) and magnetic interaction between the planet and such a disc (Takata & Stevenson 1996; Batygin 2018). We do not model these processes and merely assume that they are efficient enough that the planet contracts on a KH time-scale.

### 3.1.2 Post-runaway stage 2: fully convective

As the planet shrinks, it must radiate away an accretion flux  $L/(4\pi R^2) \propto M^2/(t_{\text{hydro}} R^3)$  given by (8) that increases; see the appendix, in particular equations (A1) and (A4), for why the factor of  $R^3$  dominates. To meet this need, the optical depth at the rcb decreases (so that  $L/(4\pi R^2) = \sigma T_0^4/\tau$  increases). When  $\tau = 1$ , the planet is no longer able to radiate away the accretional energy with a radiative layer at nearly the nebular temperature  $T_0$ . The planet is now fully convective with a rising photospheric temperature  $T > T_0$  given by

$$L = 4\pi R^2 \sigma T^4 = \frac{GM^2}{t_{\text{hydro}} R}. \quad (10)$$

There has been a longstanding debate in the literature as to whether the temperature at the planet's photosphere is correctly given by equation (10) (see Berardo et al. 2017 for a review). Since the planet radius lies inside the Bondi radius, the infalling gas is supersonic and has its bulk kinetic energy converted into heat through an accretion shock. The equilibrium temperature behind the shock depends on how efficiently the post-shock gas cools, and can range from  $T_0$  (isothermal with the nebula; this would be the case if all the post-shock gas lost its energy to photons that escaped without thermalizing) to  $T$  as given by equation (10) (complete thermal equilibrium between radiation and matter in the post-shock region). For more details, see section 2.1 of Commerçon et al. (2011) and also Zel'dovich & Raizer (1967). These two limits lead to different specific entropies, and by extension different cooling luminosities after planets stop accreting ('cold starts' vs. 'hot starts'; Fortney et al. 2005, 2008; Marley et al. 2007; Spiegel & Burrows 2012; Berardo et al. 2017). Deciding between the two limits during the radiative-envelope stage (Section 3.1.1) is not important because the accretion luminosity  $L < 4\pi R^2 \sigma T_0^4$  as given by equation (8) cannot lift the photospheric temperature  $T$  substantially above the nebular floor  $T_0$ . For the subsequent fully convective stage, we assume the hot limit as given by equation (10) holds. Our calculation is thus compatible with classical high-entropy hot starts (such models also seem to better fit directly imaged planets, although this might be a result of selection bias; Bowler 2016; Snellen & Brown 2018; Wang et al. 2018; Dupuy et al. 2019; Nielsen et al. 2019). Specifically, in our

model  $t_{\text{cool}}$  equals  $t_{\text{hydro}}$ , and both equal  $t_{\text{disc}}$  when the planet reaches its final mass. The planet's formation entropy is therefore the same as that of a classical hot start evaluated at an age of  $t_{\text{disc}}$  (hot-start models cool down from arbitrarily hot initial conditions which are eventually forgotten; see e.g. Fortney et al. 2008). The detailed radiation-hydrodynamics calculations of Marleau et al. (2017) and Marleau et al. (2019) rule out cold starts and yield temperatures within an order-unity factor of our equation (10).

The evolution of  $R(M)$  during the convective-envelope stage is found numerically by asserting the fully-convective condition: at the rcb,

$$\tau(M, R, T) = 1 \quad (11)$$

with  $T$  satisfying  $t_{\text{cool}} = t_{\text{hydro}}$  according to equation (10), and with the left-hand side calculated using equation (7) (but now with  $T > T_0$ ).

## 4 EVOLUTIONARY TRACKS

Figs 1 and 2 show how our nominal planet's radius, luminosity, and photospheric temperature evolve with mass and with time. At a mass of  $M_0 = 0.5 M_J$ , the planet transitions from cooling-limited runaway growth at  $R = R_B$  (dot-dashed red lines; Section 2) to hydrodynamically-limited mass growth on a time-scale  $t_{\text{hydro}} \propto M^\beta$  and concurrent contraction to  $R < R_B$  (Section 3). Results are plotted for two values of  $\beta$  describing accretion in gaps opened in high viscosity discs ( $\beta = 3$ ) and low viscosity discs ( $\beta = 15$ ) (see GC19).

As the planet contracts, its interior heats up ( $k_B T_c \sim GM\mu/R$ ), causing first molecular hydrogen to dissociate and next atomic hydrogen to ionize. These two phase transitions lower the adiabatic index  $\gamma$  and thereby accelerate contraction (see equations A1 and A7); the photospheric temperature and luminosity jump during these transitions.<sup>3</sup> As a guide to interpreting some of the behaviour exhibited in Fig. 1, we provide in the appendix an analytical derivation of the asymptotic radius and luminosity evolution in two regimes: prior to dissociation, and after the interior is fully ionized.

The filled circles in Figs 1 and 2 mark the transition to fully convective envelopes whose photospheric temperatures exceed the nebular temperature  $T_0$  (see bottom panels, and Section 3.1.2). From this point onward ( $\sim 10^5$  years after the end of runaway), the evolution does not depend on our choice of  $T_0$ . The filled squares indicate the planet's final mass, attained when  $t_{\text{hydro}} = M/\dot{M}$  equals the nominal gas disc lifetime  $t_{\text{disc}} = 3$  Myr (we extend the curves in Fig. 2 to consider  $t_{\text{disc}}$  up to  $10^7$  years). The filled squares mark where our calculation ends and where cooling models for isolated (non-accreting) planets begin. The case  $\beta = 3$  naturally leads to a higher final mass. In Fig. 1, we truncate the curves at  $R = 2R_J$ , the approximate radius for which electron degeneracy and Coulomb interactions, neglected in our equation of state, become important. Since the planet reaches its final mass at  $R \approx 10R_J$ , it is safely modelled as an ideal gas while accreting (and for some time after accretion ceases).

<sup>3</sup> Self-gravitating atmospheres become dynamically unstable when  $\gamma < 4/3$  in a large enough portion of the planet. Therefore, the phase transitions might occur on even shorter time-scales than are shown in Fig. 2 (namely dynamical time-scales).



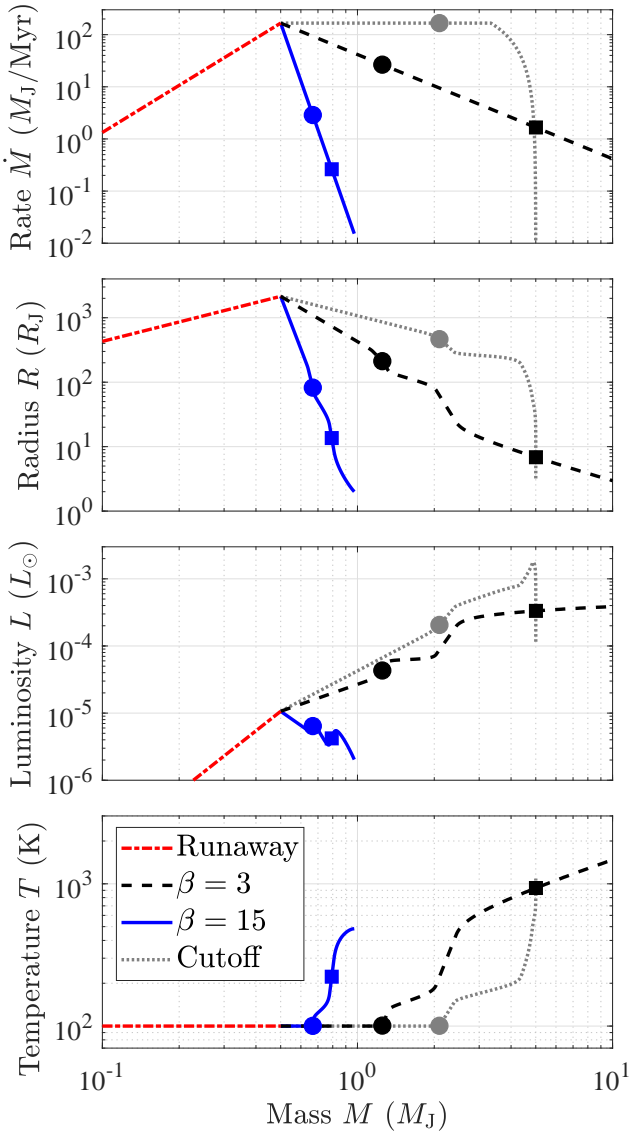


**Figure 1.** The accretion rate, radius, luminosity, and photospheric temperature of a planet as it grows in mass. Initially, for  $M < M_0 = 0.5M_J$ , the planet extends to the Bondi radius and accretes mass at a runaway pace set by the Kelvin–Helmholtz time  $t_{\text{cool}}$ , evaluated using an rcB opacity  $\kappa = 0.1 \text{ cm}^2 \text{ g}^{-1}$  (dot–dashed red lines; see Section 2). For  $M > M_0$ , accretion is limited by the hydrodynamical time  $t_{\text{hydro}} \equiv M/\dot{M} \propto M^\beta$ , where  $\beta = 3$  pertains to high disc viscosities and  $\beta = 15$  to low ones (GC19). During this stage the planet simultaneously accretes mass and contracts, satisfying  $t_{\text{cool}}(M, R) = t_{\text{hydro}}(M)$ , an equation we solve in Section 3.1. Vertical kinks in the curves correspond to hydrogen dissociation and ionization in the planet’s interior. Filled circles mark the transition to a fully-convective envelope, after which  $T$  equals the thermalized accretion value given by equation (10) and rises above the nebular  $T_0 = 100 \text{ K}$ . Filled squares mark the planet’s final mass, when  $t_{\text{hydro}}$  exceeds the protoplanetary gas disc’s lifetime  $t_{\text{disc}} = 3 \text{ Myr}$ . The dotted grey line depicts an additional model in which the accretion rate is kept constant and then artificially cut off to reach a final mass of  $5M_J$ .

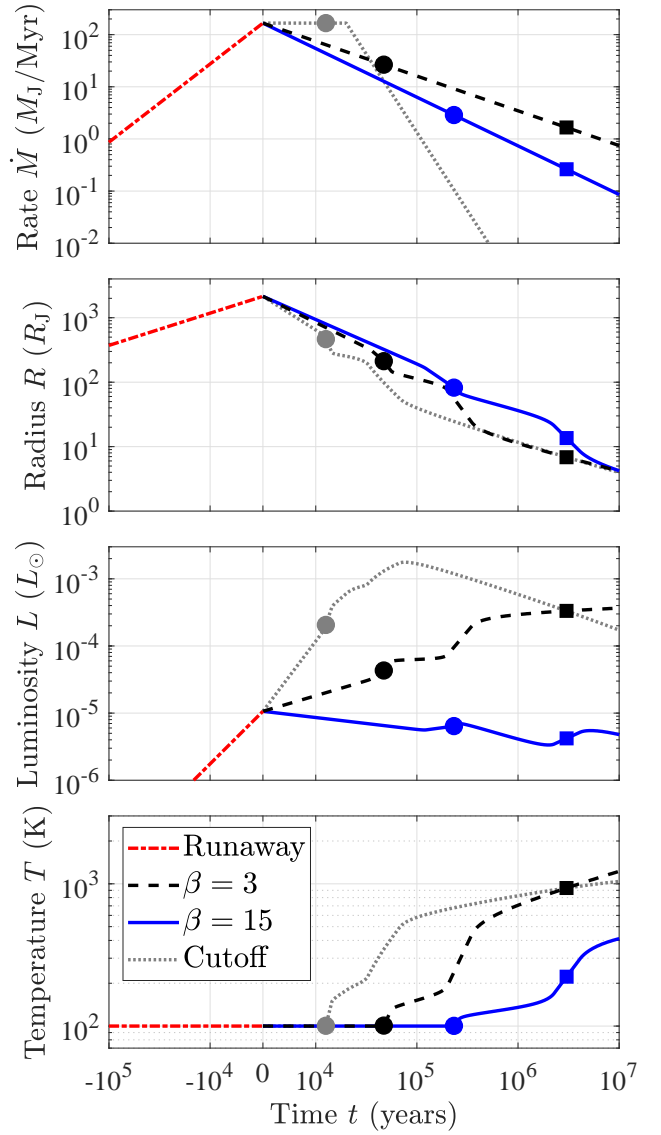


**Figure 2.** Same as Fig. 1, but as a function of time. The transition from runaway cooling to gap-mediated hydrodynamic accretion is marked by  $t = 0$ ; at this moment,  $M = M_0 = 0.5M_J$ ,  $R = R_B$ , and  $t_{\text{cool}} = t_{\text{hydro}} \approx 3 \times 10^3 \text{ yrs}$  (equation 4 with  $\kappa = 0.1 \text{ cm}^2 \text{ g}^{-1}$ ). The time axis is logarithmic for both  $t > 0$  and  $t < 0$ , but with times  $|t| < t_{\text{cool}}(M_0)$  near the transition not plotted. During runaway cooling,  $-t \propto M^{-2}$  for  $M \ll M_0$  (Section 2). During the hydrodynamic phase,  $+t \propto M^\beta$  (Section 3). The accretion rate of the ‘cutoff’ model is set to decay as  $\dot{M} \propto t^{-3}$ . During the decay  $M/\dot{M} \gg t$ , and the contraction luminosity surpasses the accretion luminosity.

Although the accretion rate peaks at the end of runaway (see discussion surrounding equation 5 and the top panels of Figs 1 and 2), the luminosity does not necessarily peak there;  $L$  can either decrease or increase after the planet transitions from cooling-limited to hydro-limited accretion, depending on the value of  $\beta$ . This result can be understood analytically (see equations A3 and A8). A few Myrs after the end of runaway, when accreting planets are most likely to be observed, the  $\beta = 3$  and  $\beta = 15$  models are separated by two orders of magnitude in luminosity:  $L \approx 4 \times 10^{-4} L_\odot$

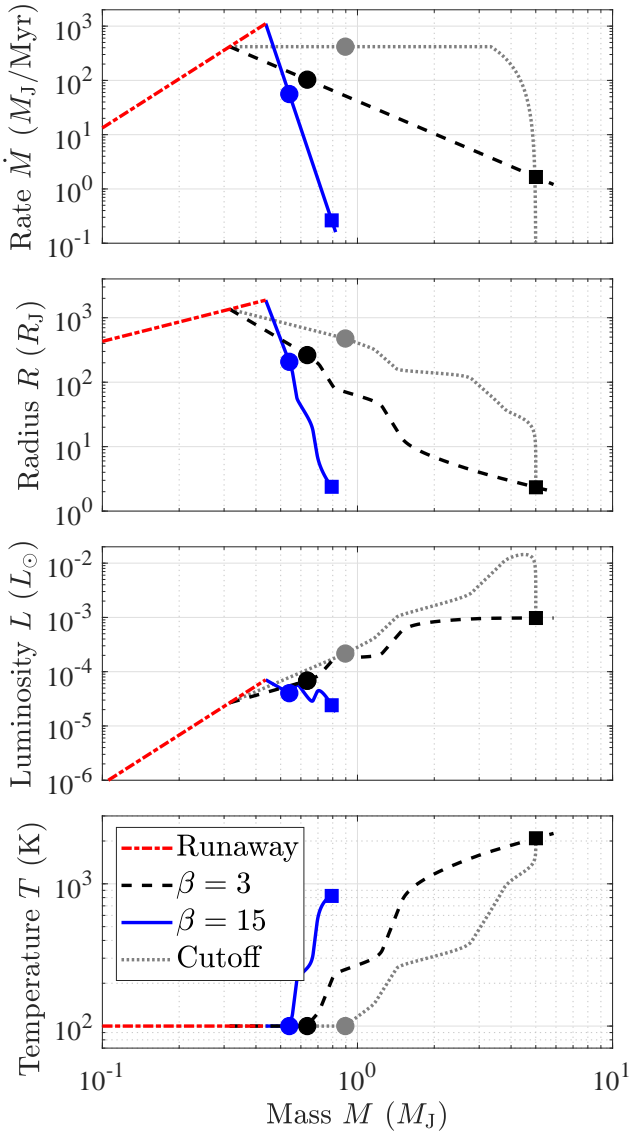


**Figure 3.** Same as Fig. 1, but with  $\kappa = 10^{-2} \text{ cm}^2 \text{ g}^{-1}$  appropriate for a dust-free rcb. We keep the same final masses as in Fig. 1 by changing  $M_0$ :  $M_0(\beta = 3) \approx 0.32M_J$  and  $M_0(\beta = 15) \approx 0.44M_J$ .

and  $L \approx 4 \times 10^{-6} L_\odot$ , respectively, where  $L_\odot$  is the solar luminosity. These luminosities are roughly constant while the planet accretes from  $1 \text{ Myr} \lesssim t \lesssim 10 \text{ Myr}$ .

Our luminosity evolution lacks the distinctive bright  $\gtrsim 10^{-3} L_\odot$  flash found in many earlier computations (Bodenheimer et al. 2000; Hubickyj et al. 2005; Marley et al. 2007; Mordasini et al. 2012). This brief flash is an artefact of the ad hoc way that runaway growth is terminated, as pointed out by Bodenheimer et al. (2000). In these models, the prescribed accretion rate is kept near its maximal value during most of the planet’s contraction and then switched off rapidly so as to arrive at a final mass near Jupiter (see e.g. fig. 2 of Mordasini et al. 2012). The sharp rise in luminosity ( $L \sim GM\dot{M}/R$ ) occurs because  $R$  is allowed to drop while  $\dot{M}$  is still pinned by hand to its maximum value. By contrast, in our models,  $R$  and  $\dot{M}$  decrease simultaneously, resulting in a flatter luminosity curve. The

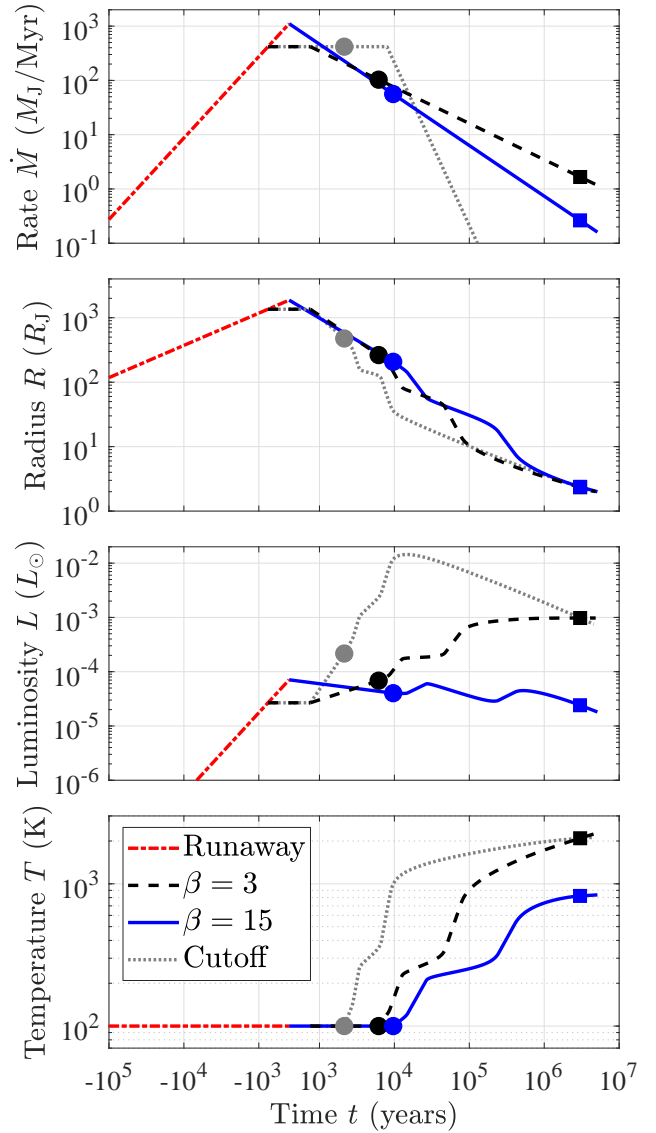


**Figure 4.** Same as Fig. 2, plotted with the same logarithmic time axis excised for times near  $t = 0$ , but computed using  $\kappa = 10^{-2} \text{ cm}^2 \text{ g}^{-1}$  (so this figure is also the same as Fig. 3, plotted here as a function of time). Compared to  $\beta = 15$ , the minimal KH cooling time-scale for the  $\beta = 3$  model is now longer and so its transition to the hydrodynamic phase is slower; hence the flat segment of the dashed curve that extends just past  $t = 0$ .

accretion rate in Mordasini et al. (2017) also drops roughly as a power law from its maximal value, yielding a luminosity curve that lacks the short bright flash (their fig. 1). For further illustration, we add a third model (dotted grey line) to Figs 1 and 2. This model terminates the accretion in a similar way to previous studies, demonstrating that the bright flash is an artefact. We choose to cut off this model at the same final mass as our  $\beta = 3$  model to emphasize that the radius and luminosity of a planet at a given age and mass do not depend on its accretion history—they are determined solely by KH cooling. After such an unphysically sharp cutoff,  $M/\dot{M} \gg t$  and the planet cools and contracts essentially as if it were not accreting at all.

## 5 DEPENDENCE ON OPACITY

From Figs 1 and 2, the photospheric temperature (= rcb temperature) can approach the dust sublimation point. Grain growth and sedimentation in planetary envelopes can also decrease the dust opacity (Movshovitz et al. 2010; Mordasini 2014; Ormel 2014). Furthermore, the low opacities of dust-free gas may explain how the exceptionally voluminous atmospheres of low-mass ‘super-puff’ planets accreted (Lee & Chiang 2016, their section 4). For these reasons we are motivated to repeat our computation with a lower rcb opacity.

Figs 3 and 4 are the same as Figs 1 and 2 but calculated using  $\kappa = 10^{-2} \text{ cm}^2 \text{ g}^{-1}$  which roughly characterizes dust-free gas for our temperatures and pressures (Freedman et al. 2008). Cooling faster with a lower opacity, planets contract to approximately 2–3  $R_J$  during the last few Myrs of their formation. This result reproduces previous calculations that employed similar opacities (e.g. Mordasini et al. 2012) and can be understood using equation (A9): for a given mass and age, the radius scales approximately as  $R \propto \kappa^{8/17}$ . Below about  $2R_J$ , our neglect of degeneracy pressure and Coulomb interactions (‘cold terms’) in the equation of state renders our calculation less reliable (Jupiter-mass planets have a minimum ‘cold’ radius of about  $R_J$ ).

Giant planets newly emerging from their parent discs are commonly assumed to have  $R \approx 2R_J$  (e.g. Eisner 2015; Zhu 2015). Our analysis shows that this assumption is justified only for dust-free atmospheres. In Section 6 we further explore the impact of  $\kappa$  on the interpretation of observations.

## 6 INTERPRETING OBSERVATIONS

There are currently several candidates for planets that are still accreting gas from their parent circumstellar discs (Sallum et al. 2015; Guidi et al. 2018; Reggiani et al. 2018; Wagner et al. 2018; Haffert et al. 2019; cf. Mendigutía et al. 2018; Currie et al. 2019). The observed luminosity  $L$  of a given candidate is usually translated into a constraint on  $M\dot{M}$  (the planet’s mass times its accretion rate) using  $L = GM\dot{M}/R$ , where the planet’s radius  $R$  is either assumed to be 1–2  $R_J$  (Eisner 2015; Zhu 2015), or left as a free parameter. Planetary radii during post-runaway accretion are indicated in Figs 2 and 4; in particular, for high envelope opacities appropriate to dusty gas, planets a few Myrs old could still be several times larger than Jupiter.

In Section 3 we explained that the planet cools and contracts on the same time-scale that it grows in mass:  $t_{\text{cool}}(M, R) = t_{\text{hydro}} \equiv M/\dot{M}$ . From this we computed  $R(M, \dot{M})$  and  $L(M, \dot{M})$  for specific accretion rates  $\dot{M}(M)$  (equivalently  $\dot{M}(t)$ ); the latter were physically motivated by how planets accrete from within disc gaps. While accretion luminosities can be factors of  $\sim 10^2$  higher in viscous discs than in inviscid ones, we caution that observing a high luminosity does not necessarily rule out inviscid discs, as all the curves in Figs 1 and 2 shift as a function of the parameter  $M_0$ , the mass for which the planet transitions from cooling-limited to hydrodynamically-limited accretion. To illustrate this degeneracy, increasing  $M_0$  from our nominal value of  $0.5M_J$  to  $3M_J$  in Fig. 1 would extend the runaway line and increase post-runaway luminosities by a factor of  $10^2$  (see also the last

paragraph of the appendix). That said, the observed planet candidate orbiting MWC 758 is so bright ( $L > 10^{-3}L_\odot$ ; Reggiani et al. 2018) that we cannot reconcile it with our  $\beta = 15$  and  $\kappa = 0.1 \text{ cm}^2 \text{ g}^{-1}$  inviscid track (but the  $\beta = 3$  viscous track is compatible). Given the candidate’s distance from its host star of  $\sim 20$  au, we estimate using the disc model of GC19 that  $M_0 \approx 1M_J$  if  $\beta = 15$  (see also the footnote in Section 3), which implies that its peak luminosity does not exceed  $10^{-4}L_\odot$ . We will give another reason why the inviscid scenario is not compatible with MWC 758 when we infer its mass below.

In Figs 5 and 6 we exploit the same equality  $t_{\text{cool}}(M, R) = t_{\text{hydro}} = M/\dot{M}$  to calculate  $R$  for an arbitrary combination of  $M$  and  $\dot{M}$ . That is, we replace  $t_{\text{hydro}}$  with  $M/\dot{M}$  in equations (9)–(11) and solve for  $R(M, \dot{M})$ . This approach dispenses with the need to prescribe  $\dot{M}(M)$  (i.e.  $\beta$  in equation 5 need not be specified). The curves of constant  $R$  in Figs 5 and 6 are nearly parallel with the curves of constant accretion time-scale  $M/\dot{M}$ , more so at long  $M/\dot{M}$ ; planets simply contract as they age (see also Figs 2 and 4). For our high-opacity (dusty) model, planets contract to  $\sim 7R_J$  at  $M/\dot{M} = 3$  Myr and to  $\sim 4R_J$  at  $M/\dot{M} = 10$  Myr. For our low-opacity (dust-free) model, the canonical 1–2  $R_J$  is attained for  $M/\dot{M} \gtrsim 3$  Myr; the rate of contraction at longer times is overestimated because of our neglect of cold terms in the equation of state.

In Fig. 7 we use the  $R$  values from Figs 5 and 6 to calculate accretion luminosities  $L$  as a function of  $M$  and  $\dot{M}$ . A planet candidate’s measured accretion luminosity falls along a contour of constant  $L$  (shown in blue for high  $\kappa$  and red for low  $\kappa$ ), constraining a combination of  $M$  and  $\dot{M}$ —this combination is not merely the product  $M\dot{M}$  because we do not assume a constant  $R$  but rather calculate its variation. This joint constraint can be resolved into separate individual constraints on  $M$  and  $\dot{M}$  if we also measure the system age and assume that it equals  $M/\dot{M}$ . We perform this exercise on four candidate planets: PDS 70 b (Keppler et al. 2018; Wagner et al. 2018), PDS 70 c (Haffert et al. 2019), the infrared point source in HD 163296 (Guidi et al. 2018), and the infrared companion to MWC 758 (Reggiani et al. 2018). These systems appear in Fig. 7 either as blue circles or red squares, depending on whether they are interpreted using our high- $\kappa$  or low- $\kappa$  model, respectively. Since  $R$  scales in our numerical model as  $\kappa^{0.5}$  (cf. equation A9), the inferred  $M\dot{M} = RL/G$  varies with  $R$  and thus  $\kappa$  at a fixed measured luminosity; hence the red points must be paired with the red contours, and likewise for blue.

At face value, Fig. 7 indicates the planet candidates around PDS 70 and HD 163296 are between  $\sim 1$ – $3 M_J$  and are accreting at rates of  $\sim 0.2$ – $0.6 M_J/\text{Myr}$ ; in the case of MWC 758,  $M \sim 5$ – $10 M_J$  and  $\dot{M} \sim 3$ – $7 M_J/\text{Myr}$ . There are, of course, numerous systematic uncertainties underlying these estimates; perhaps the most glaring is the poorly calibrated and understood conversion of  $H\alpha$  luminosity into bolometric accretion luminosity (Rigliaco et al. 2012; Wagner et al. 2018). We describe in the caption to Fig. 7 the various assumptions we made to assign ages and luminosities to our four objects. It is nevertheless interesting and reassuring to infer from Figs 5–7 a radius for PDS 70 b that lies between  $1.8R_J < R < 5R_J$ , a range that overlaps with the radii fitted to spectral energy distributions (Müller et al. 2018). In particular, our high- $\kappa$  model yields a more slowly contracting planet and can explain why some of the fitted radii ex-

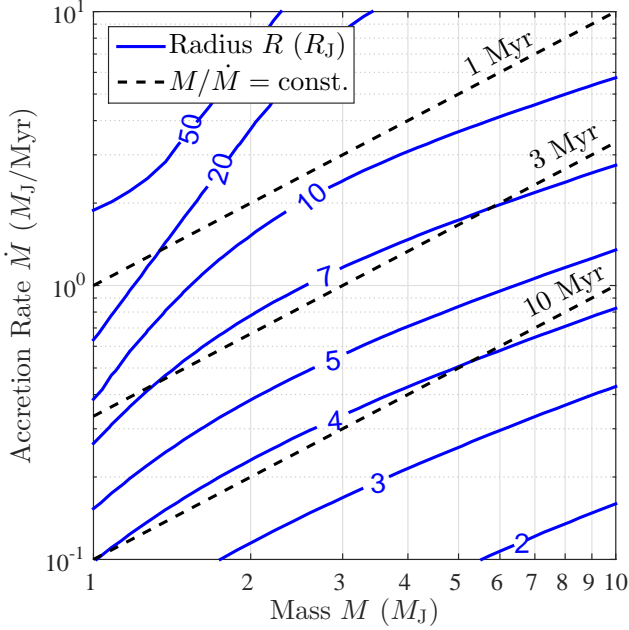


**Figure 5.** Contours of constant radius  $R(M, \dot{M})$  (solid blue lines) for an accreting protoplanet with a dusty rcb opacity  $\kappa = 0.1 \text{ cm}^2 \text{ g}^{-1}$ . Radii are computed by equating the planet’s Kelvin–Helmholtz cooling time to its growth time:  $t_{\text{cool}}(M, R) = t_{\text{hydro}} \equiv M/\dot{M}$ . This is the same equation used to compute previous figures, but it is used here with an arbitrary  $\dot{M}$  (i.e. no relation  $\dot{M}(M)$  and in particular no  $\beta$  are assumed). Dashed black lines indicate mass doubling times  $M/\dot{M}$ .

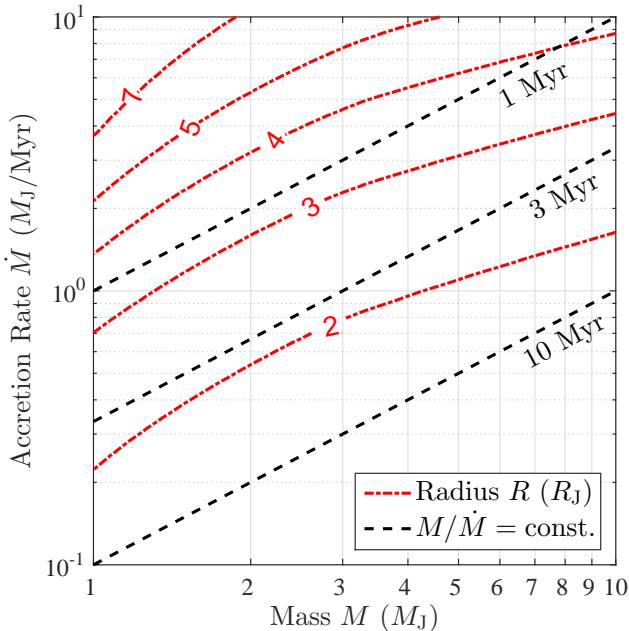


**Figure 6.** Same as Fig. 5, but with a dust-free rcb opacity  $\kappa = 10^{-2} \text{ cm}^2 \text{ g}^{-1}$ . The constant-radius contours for this low- $\kappa$  model are dot-dashed and coloured red for consistency with the low- $\kappa$  curves in Fig. 7.

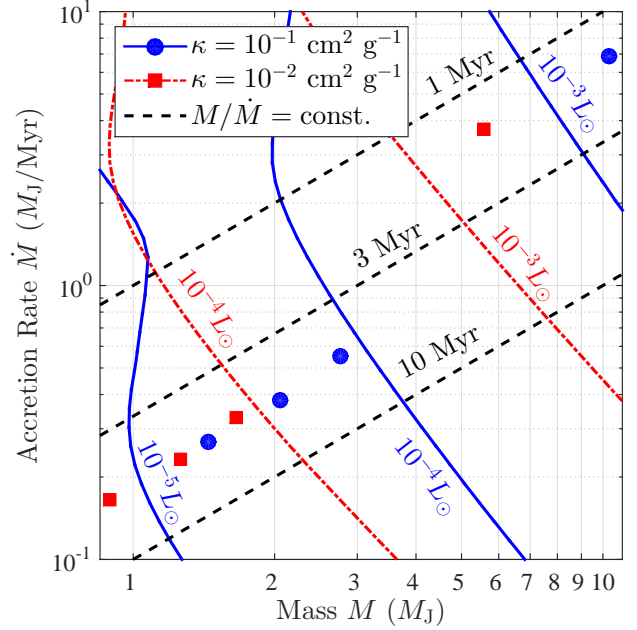


**Figure 7.** Contours of constant accretion luminosity  $L(M, \dot{M}) = GM\dot{M}/R$  computed for high  $\kappa = 0.1 \text{ cm}^2 \text{ g}^{-1}$  (solid blue; the corresponding  $R$  values are calculated in Fig. 5) and low  $\kappa = 10^{-2} \text{ cm}^2 \text{ g}^{-1}$  (dot-dashed red;  $R$  calculated in Fig. 6). Symbols denote four candidate planets, plotted using their measured luminosities  $L$  (so red squares are plotted in relation to red luminosity contours, and blue circles are in relation to blue contours) and ages  $t$  that we equate to mass doubling times  $M/\dot{M}$  (so plotted in relation to the dashed black lines). The plot maps  $(L, t = M/\dot{M})$  to  $(M, \dot{M})$  and thus can be used to infer the masses and accretion rates of observed planets. From left to right, the planet candidates orbit PDS 70 (c and b; Haffert et al. 2019; Keppler et al. 2018; Wagner et al. 2018), HD 163296 (Guidi et al. 2018), and MWC 758 (Reggiani et al. 2018). For PDS 70 we take the nominal age estimate from Müller et al. (2018) and the largest extinction assumed by Wagner et al. (2018); weaker extinctions imply lower  $L$  and therefore lower  $M$ . For PDS 70 b we assume the same conversion from  $H\alpha$  luminosity to bolometric  $L$  as in Wagner et al. (2018), and for PDS 70 c we scale from b using their K-band flux ratio, observed to be equal to the  $H\alpha$  ratio (Haffert et al. 2019). For MWC 758 we assume the youngest age estimate; older ages lead to higher masses beyond the scope of our high- $\kappa$  model. In summary, the following values are used for the four objects in the plot (from left to right):  $t/\text{Myr} = (5.4, 5.4, 5, 1.5)$  and  $L/(10^{-5} L_{\odot}) = (2.1, 4.4, 8.2, 180)$ .

ceed  $2R_J$ , in contrast to low- $\kappa$  models (e.g. Mordasini et al. 2012). Our mass and radius ranges for PDS 70 b are also consistent with the atmospheric ‘planet alone’ models of Christiaens et al. (2019b) as fitted to the observed K-band spectrum; by comparison, their ‘planet + CPD’ model yields a more massive best fit of  $10 M_J$ . In addition, our inferred accretion rate agrees with the upper limit estimated from the non-detection of  $\text{Br}\gamma$  emission by Christiaens et al. (2019a).

Earlier we saw that the high luminosity of the companion to MWC 758 could be explained by post-runaway accretion in a viscous disk but not in an inviscid one. The high inferred mass of MWC 758 gives another reason to disfavour its formation in an inviscid disc. If  $\beta = 15$ , the planet mass cannot grow much beyond the transition mass  $M_0$ , at most doubling (Fig. 1 and fig. 3 of GC19 at 20 au). For MWC



758, the transition mass of  $M_0 \approx 1M_J$  and the present-day inferred mass of 5–10  $M_J$  (Fig. 7) are too far separated to be reproduced by an inviscid evolution.

## 7 SUMMARY

Direct imaging is enabling the detection of planets still accreting gas from their host circumstellar discs. The luminosities of such planets are a key observable; they constrain mass accretion rates and by extension planet formation theories.

What is essential to understand is how the planet’s gas accretion rate  $\dot{M}$  drops from its runaway value, i.e. how runaway stops while the planet is still embedded within its parent disc. Previous treatments artificially limited the runaway  $\dot{M}$  to some maximum value, and then lowered  $\dot{M}$  to zero over an arbitrary and unrealistically short time-scale, all to yield a prescribed final mass (Marley et al. 2007; Mordasini et al. 2012). What we have posited instead is that gas accretion decays on a time-scale comparable to the lifetime of the gas disc. Post-runaway gas accretion may actually be the longest phase of gas giant formation.

What stops runaway? The opening of gaps is one possibility. In the post-runaway era, gas accretion continues, but at a rate diminished by the reduction of disc density by repulsive Lindblad torques. Ginzburg & Chiang (2019) show that gap opening causes the planet’s mass doubling time-scale  $M/\dot{M}$  to increase with increasing planet mass  $M$ , with the scaling dependent on disc viscosity. In high-viscosity discs,  $M/\dot{M} \propto M^3$ ; in low-viscosity discs where gaps are deeper,  $M/\dot{M} \propto M^{15}$ . We experimented here with both scalings and found that they yielded qualitatively different luminosity evolutions. In the high-viscosity case, the accretion luminosity  $L$  continues to rise past runaway all the way to disc dispersal; for our nominal parameters,  $L \sim 10^{-4}$ – $10^{-3}L_\odot$  during the last few Myrs of the disc’s life. In the low-viscosity case, the luminosity drops post-runaway to  $10^{-6}$ – $10^{-5}L_\odot$ . The divergence of luminosity tracks is solely the result of different post-runaway accretion histories (which in turn stem from different disc viscosities  $\alpha$ ). The evolution during and prior to runaway is otherwise identical between the two tracks, as is the treatment of the accretion shock, which we do not take to be isothermal with the nebula, but which instead thermalizes at the blackbody temperature. In this sense, our calculations are compatible with ‘hot start’ models for post-formation cooling (see Marleau et al. 2017 and Marleau et al. 2019 for details).

The order-of-magnitude differences in  $L$ , which can be understood analytically (see the appendix), persist for Myrs, and highlight the importance of accurately modelling the terminal phase of nebular accretion. We established in Section 3 that during this final phase, the planet contracts to a radius  $R$  such that the Kelvin–Helmholtz cooling time  $GM^2/(RL)$  is slaved to the (externally controlled) growth time  $M/\dot{M}$ . From this equality of time-scales follows the planet’s radius evolution with time  $R(t)$ , and by extension the evolution of luminosity  $L(t) = GM^2/(Rt)$  and photospheric temperature  $T(t) = [L/(4\pi\sigma R^2)]^{1/4}$ . Surface temperatures start from the ambient nebular temperature during runaway, and increase post-runaway to values ranging from ~200–2000 K.

Even without specifying the full accretion history  $\dot{M}(M)$ ,

we can solve for the instantaneous  $R$ ,  $L$ , and  $T$  given the instantaneous  $M$  and  $\dot{M}$ . The condition that the planet’s Kelvin–Helmholtz cooling time equals its growth time, together with conditions at the radiative-convective boundary, enables us to map  $M$  and  $\dot{M}$  to  $R$  (Figs 5 and 6) and  $L$  (Fig. 7). In the literature it is often assumed that an accreting gas giant has  $R \approx 2R_J$ . Our dust-free, low-opacity models can produce such a radius, but our dusty, high-opacity models yield radii that are generally larger by factors of a few. Deciding between these models requires that we understand how dust evolves in planetary atmospheres.

Finally, we applied our theory to the planet candidates in PDS 70, HD 163296, and MWC 758. From their observed luminosities  $L$  and ages  $t$  we inferred masses  $M \sim 1$ – $10 M_J$  and accretion rates  $\dot{M} \sim 0.1$ – $10 M_J/\text{Myr}$  (Figure 7). These inferences rely on the assumption that observed system ages can be interpreted as planet mass doubling times:  $t = M/\dot{M}$ . We infer a radius for PDS 70 b between 1.8– $5R_J$  that is compatible with radius determinations from spectral energy distributions (Müller et al. 2018); values greater than  $2R_J$  are made possible by higher opacities from dust which slow planetary contraction.

Future work needs to confront the angular momentum barrier that spinning envelopes somehow surmount in order to contract to their observed sizes. The formation of rotationally supported circumplanetary discs (CPDs; e.g. Ward & Canup 2010) and associated magnetic torques (Takata & Stevenson 1996; Batygin 2018) are probably part of this story. While CPDs yield spectral energy distributions that would differ in detail from those of the disc-less planets that we have considered here (e.g. Szulágyi et al. 2019), bolometric luminosities of CPDs and accreting planets should be comparable (an accreting planet of radius  $R$  has the same bolometric luminosity as a disc accreting at the same rate to an inner boundary layer of the same radius  $R$ ). Inferences of planet properties based on bolometric luminosities, like the kind made in our Fig. 7, should be robust in this sense.

## ACKNOWLEDGEMENTS

We thank Ian Czekala, Ruobing Dong, Josh Eisner, Gabriel-Dominique Marleau, Mark Marley, Christoph Mordasini, Diana Powell, and Jason Wang for comments and discussions. We also thank the anonymous reviewer for suggestions which improved the paper. SG is supported by the Heising-Simons Foundation through a 51 Pegasi b Fellowship.

## REFERENCES

- Alexander R., Pascucci I., Andrews S., Armitage P., Cieza L., 2014, *Protostars and Planets VI*, pp 475–496
- Batygin K., 2018, *AJ*, **155**, 178
- Bell K. R., Lin D. N. C., 1994, *ApJ*, **427**, 987
- Berardo D., Cumming A., Marleau G.-D., 2017, *ApJ*, **834**, 149
- Bodenheimer P., Pollack J. B., 1986, *Icarus*, **67**, 391
- Bodenheimer P., Hubickyj O., Lissauer J. J., 2000, *Icarus*, **143**, 2
- Bowler B. P., 2016, *PASP*, **128**, 102001
- Bryden G., Chen X., Lin D. N. C., Nelson R. P., Papaloizou J. C. B., 1999, *ApJ*, **514**, 344
- Christiaens V., et al., 2019a, *MNRAS*, **486**, 5819

- Christiaens V., Cantalloube F., Casassus S., Price D. J., Absil O., Pinte C., Girard J., Montesinos M., 2019b, *ApJ*, **877**, L33
- Commerçon B., Audit E., Chabrier G., Chièze J. P., 2011, *A&A*, **530**, A13
- Currie T., et al., 2019, arXiv e-prints,
- D’Alessio P., Calvet N., Hartmann L., 2001, *ApJ*, **553**, 321
- D’Angelo G., Kley W., Henning T., 2003, *ApJ*, **586**, 540
- Dupuy T. J., Brandt T. D., Kratter K. M., Bowler B. P., 2019, *ApJ*, **871**, L4
- Edgar R., 2004, *New Astron. Rev.*, **48**, 843
- Eisner J. A., 2015, *ApJ*, **803**, L4
- Fortney J. J., Marley M. S., Hubickyj O., Bodenheimer P., Lissauer J. J., 2005, *Astronomische Nachrichten*, **326**, 925
- Fortney J. J., Marley M. S., Saumon D., Lodders K., 2008, *ApJ*, **683**, 1104
- Freedman R. S., Marley M. S., Lodders K., 2008, *ApJS*, **174**, 504
- Ginzburg S., Chiang E., 2019, *MNRAS*, **487**, 681
- Ginzburg S., Sari R., 2015, *ApJ*, **803**, 111
- Ginzburg S., Sari R., 2018, *MNRAS*, **479**, 1986
- Ginzburg S., Schlichting H. E., Sari R., 2016, *ApJ*, **825**, 29
- Goldreich P., Tremaine S., 1980, *ApJ*, **241**, 425
- Goodman J., Rafikov R. R., 2001, *ApJ*, **552**, 793
- Guidi G., et al., 2018, *MNRAS*, **479**, 1505
- Haffert S. Y., Bohn A. J., de Boer J., Snellen I. A. G., Brinchmann J., Girard J. H., Keller C. U., Bacon R., 2019, *Nature Astronomy*, p. 329
- Harris A. W., 1978, in Lunar and Planetary Science Conference. pp 459–461
- Hubickyj O., Bodenheimer P., Lissauer J. J., 2005, *Icarus*, **179**, 415
- Ikoma M., Nakazawa K., Emori H., 2000, *ApJ*, **537**, 1013
- Keppler M., et al., 2018, *A&A*, **617**, A44
- Kley W., 1999, *MNRAS*, **303**, 696
- Lee E. J., 2019, *ApJ*, **878**, 36
- Lee E. J., Chiang E., 2015, *ApJ*, **811**, 41
- Lee E. J., Chiang E., 2016, *ApJ*, **817**, 90
- Lee E. J., Chiang E., Ormel C. W., 2014, *ApJ*, **797**, 95
- Lee E. J., Chiang E., Ferguson J. W., 2018, *MNRAS*, **476**, 2199
- Lin D. N. C., Papaloizou J. C. B., 1993, in Levy E. H., Lunine J. I., eds, Protostars and Planets III. pp 749–835
- Lissauer J. J., Hubickyj O., D’Angelo G., Bodenheimer P., 2009, *Icarus*, **199**, 338
- Lubow S. H., Seibert M., Artymowicz P., 1999, *ApJ*, **526**, 1001
- Machida M. N., Kokubo E., Inutsuka S.-I., Matsumoto T., 2010, *MNRAS*, **405**, 1227
- Mamajek E. E., 2009, in Usuda T., Tamura M., Ishii M., eds, American Institute of Physics Conference Series Vol. 1158, American Institute of Physics Conference Series. pp 3–10 ([arXiv:0906.5011](https://arxiv.org/abs/0906.5011)), doi:10.1063/1.3215910
- Marleau G.-D., Klahr H., Kuiper R., Mordasini C., 2017, *ApJ*, **836**, 221
- Marleau G.-D., Mordasini C., Kuiper R., 2019, *ApJ*, **881**, 144
- Marley M. S., Fortney J. J., Hubickyj O., Bodenheimer P., Lissauer J. J., 2007, *ApJ*, **655**, 541
- Mendigutía I., Oudmaijer R. D., Schneider P. C., Huéramo N., Baines D., Brittain S. D., Aberasturi M., 2018, *A&A*, **618**, L9
- Mizuno H., 1980, *Progress of Theoretical Physics*, **64**, 544
- Mizuno H., Nakazawa K., Hayashi C., 1978, *Progress of Theoretical Physics*, **60**, 699
- Mordasini C., 2014, *A&A*, **572**, A118
- Mordasini C., Alibert Y., Klahr H., Henning T., 2012, *A&A*, **547**, A111
- Mordasini C., Marleau G. D., Mollière P., 2017, *A&A*, **608**, A72
- Movshovitz N., Bodenheimer P., Podolak M., Lissauer J. J., 2010, *Icarus*, **209**, 616
- Müller A., et al., 2018, *A&A*, **617**, L2
- Nielsen E. L., et al., 2019, arXiv e-prints,
- Ormel C. W., 2014, *ApJ*, **789**, L18
- Papaloizou J. C. B., Nelson R. P., 2005, *A&A*, **433**, 247
- Perri F., Cameron A. G. W., 1974, *Icarus*, **22**, 416
- Piso A.-M. A., Youdin A. N., 2014, *ApJ*, **786**, 21
- Piso A.-M. A., Youdin A. N., Murray-Clay R. A., 2015, *ApJ*, **800**, 82
- Pollack J. B., Hubickyj O., Bodenheimer P., Lissauer J. J., Podolak M., Greenzweig Y., 1996, *Icarus*, **124**, 62
- Rafikov R. R., 2006, *ApJ*, **648**, 666
- Reggiani M., et al., 2018, *A&A*, **611**, A74
- Rigliaco E., Natta A., Testi L., Randich S., Alcalà J. M., Covino E., Stelzer B., 2012, *A&A*, **548**, A56
- Sallum S., et al., 2015, *Nature*, **527**, 342
- Saumon D., Chabrier G., van Horn H. M., 1995, *ApJS*, **99**, 713
- Shakura N. I., Sunyaev R. A., 1973, *A&A*, **24**, 337
- Snellen I. A. G., Brown A. G. A., 2018, *Nature Astronomy*, **2**, 883
- Spiegel D. S., Burrows A., 2012, *ApJ*, **745**, 174
- Stevenson D. J., 1982, *Planet. Space Sci.*, **30**, 755
- Szulágyi J., Morbidelli A., Crida A., Masset F., 2014, *ApJ*, **782**, 65
- Szulágyi J., Dullemond C. P., Pohl A., Quanz S. P., 2019, *MNRAS*,
- Takata T., Stevenson D. J., 1996, *Icarus*, **123**, 404
- Tanigawa T., Ikoma M., 2007, *ApJ*, **667**, 557
- Tanigawa T., Tanaka H., 2016, *ApJ*, **823**, 48
- Wagner K., et al., 2018, *ApJ*, **863**, L8
- Wang J. J., et al., 2018, *AJ*, **156**, 192
- Ward W. R., Canup R. M., 2010, *AJ*, **140**, 1168
- Williams J. P., Cieza L. A., 2011, *ARA&A*, **49**, 67
- Zel’dovich Y. B., Raizer Y. P., 1967, Physics of shock waves and high-temperature hydrodynamic phenomena. New York: Academic Press
- Zhu Z., 2015, *ApJ*, **799**, 16

## APPENDIX A: ANALYTICAL SCALINGS

### A1 Radiative envelope

During the early stages of contraction, the planet is still too cold for hydrogen molecules to dissociate, so  $\gamma = 7/5$ . In this case the optical depth at the rcb  $\tau(M, R, T_0)$  is given by equation (3), and equation (9) can be solved analytically to yield

$$\frac{d \ln R}{d \ln M} = -\frac{\beta(\gamma - 1) + 3 - 2\gamma}{4\gamma - 5} = \begin{cases} -7/3 & \beta = 3 \\ -31/3 & \beta = 15, \end{cases} \quad (\text{A1})$$

with the normalization  $R(M_0) = R_B(M_0) \approx 2 \times 10^3 R_J$ . The luminosity is given by equation (8) and evolves as

$$\frac{d \ln L}{d \ln M} = -\frac{\beta(3\gamma - 4) + 7 - 6\gamma}{4\gamma - 5} = \begin{cases} +4/3 & \beta = 3 \\ -8/3 & \beta = 15. \end{cases} \quad (\text{A2})$$

The value of the luminosity at the end of runaway,  $L(M_0) \approx 10^{-5} L_\odot$ , with  $L_\odot$  denoting the solar luminosity, is calculated by substituting  $R(M_0) = R_B(M_0)$  in equation (8).

Interestingly, the luminosity can either decrease (if  $\beta > \beta_{\text{cr}}$ ) or increase (if  $\beta < \beta_{\text{cr}}$ ) during the planet’s contraction, depending on the value of  $\beta$ . The critical value is

$$\beta_{\text{cr}} = \frac{6\gamma - 7}{3\gamma - 4} = 7. \quad (\text{A3})$$

The analytical solutions (A1)–(A2) fit well the earliest segments of the evolutionary tracks computed numerically with a more accurate  $\gamma(\rho, T)$  (Fig. 1).

Using equations (3) and (A1), the optical depth of the

radiative envelope drops as

$$\tau \propto \frac{1}{R} \left( \frac{R}{M} \right)^{1/(\gamma-1)} \propto \begin{cases} M^{-6} & \beta = 3 \\ M^{-18} & \beta = 15 \end{cases} \quad (\text{A4})$$

from an initial value of  $\tau(M_0) = \kappa M_0 / R_{\text{B}}^2(M_0) \approx 4 \times 10^2$ . When  $\tau = 1$  is reached, the diffusive radiative layer at  $T \approx T_0$  vanishes and the planet becomes fully convective with a photospheric temperature  $T > T_0$  (Section 3.1.2).

## A2 Fully convective

Most of the radiative-envelope phase can be calculated analytically with a single  $\gamma = 7/5$  as the planet remains fully molecular (Section A1). The transition to the fully convective phase (filled circles in Figs 1 and 2) nearly coincides with the onset of molecular dissociation, so this phase can only be solved numerically (Section 3.1.2).

We can still gain some analytical intuition by modelling the final stage of post-runaway accretion, when the planet's interior is fully ionized (after the two bumps in Figs 1 and 2, which indicate dissociation and ionization). During this phase, we model the planet piecewise:  $\gamma_1 = 5/3$  in the fully dissociated and ionized interior, and  $\gamma_2 = 7/5$  in the molecular exterior where the photospheric temperature  $T$  remains below the dissociation temperature  $T_{\text{diss}} \approx 2500$  K (see Fig. 1). The dissociation temperature depends only weakly on density according to the Saha equation. This two-piece construction reduces dissociation and ionization to a single sharp transition.

The integration of equation (6) from  $T < T_{\text{diss}}$  to  $T_c > T_{\text{diss}}$  with the piecewise index yields

$$\rho_{\text{rcb}} \sim \frac{M}{R^3} \left( \frac{T}{T_{\text{diss}}} \right)^{1/(\gamma_2-1)} \left( \frac{k_{\text{B}} T_{\text{diss}} R}{GM\mu} \right)^{1/(\gamma_1-1)}. \quad (\text{A5})$$

The optical depth scales as

$$\tau = \kappa \rho_{\text{rcb}} h = \kappa \rho_{\text{rcb}} \frac{k_{\text{B}} T R^2}{GM\mu} \propto T^{\gamma_2/(\gamma_2-1)} \frac{1}{R} \left( \frac{R}{M} \right)^{1/(\gamma_1-1)}, \quad (\text{A6})$$

where  $T^4 \propto M^{2-\beta} R^{-3}$  from equations (5) and (10). By asserting that  $\tau$  equals unity, equation (A6) reads

$$\frac{d \ln R}{d \ln M} = -\frac{\beta \gamma_2 - 2\gamma_2 + 4r}{7\gamma_2 - 4 - 4r} = \begin{cases} -19/17 & \beta = 3 \\ -103/17 & \beta = 15, \end{cases} \quad (\text{A7})$$

where  $r \equiv (\gamma_2 - 1)/(\gamma_1 - 1) = 3/5$ . Using equations (5) and (10), the luminosity evolves as

$$\frac{d \ln L}{d \ln M} = \frac{2(16 - 5\beta)}{17} = \begin{cases} +2/17 & \beta = 3 \\ -118/17 & \beta = 15, \end{cases} \quad (\text{A8})$$

with the critical  $\beta_{\text{cr}} = 16/5$  during this stage.

We reiterate that equations (A7) and (A8) are applicable only after the planet's interior becomes fully ionized. Even then, these scaling relations are approximate, as they do not account for the (weak) dependence of  $T_{\text{diss}}$  on density, and treat dissociation and ionization as a single sharp transition. Nevertheless, the equations reproduce the qualitative behaviour of the radius and luminosity close to the time of disc dispersal (filled squares in Fig. 1). Moreover, equations (10) and (A6) specify the dependence of the planet's radius,

at a given time, on the opacity:

$$\frac{d \ln R}{d \ln \kappa} = \left( \frac{3}{4} \frac{\gamma_2}{\gamma_2 - 1} - \frac{1}{\gamma_1 - 1} + 1 \right)^{-1} = \frac{8}{17}, \quad (\text{A9})$$

which helps explain the results of Section 5.

Equations (A1)–(A2) and (A7)–(A8) illustrate the sensitivity of our results to  $M_0$ , the transition mass from runaway to post-runaway. Since the slopes given by these equations depend only on  $\beta$  and  $\gamma$ , the curves for different  $M_0$  are, to leading order, parallel, departing from different points along the dot-dashed red line in Fig. 1.

This paper has been typeset from a  $\text{\TeX}/\text{\LaTeX}$  file prepared by the author.